Supplementary Information

Outstanding field emission performance via superior carbon nanotubes dispersion by acoustic resonance mixing and synergistic function-oriented annealing strategy

Weiwei Yu [a], Ziqin Ai [a], Zhe Liu[b], Shulan Jiang[a, *], Zirong Tang[b], Xiaobin Zhan[b], XiuGuo Chen[b]

[a] *School of Mechanical Engineering and Electronic Information, China University of Geosciences, Wuhan, Hubei 430074, China*

[b] *State Key Laboratory of Intelligent Manufacturing Equipment and Technology, Huazhong University of Science and Technology, 1037 Luoyu Road, Wuhan, Hubei 430074, China*

1. Morphological Analysis

To validate the superior dispersion performance of the acoustic resonance mixing technology and ensure the accuracy of experimental results, we employed spin-coating to prepare three repeated samples each for ball milling samples and samples at vibration frequencies of 30 Hz, 60 Hz and 100 Hz. Optical microscopy morphological characterization was subsequently conducted on all prepared samples.

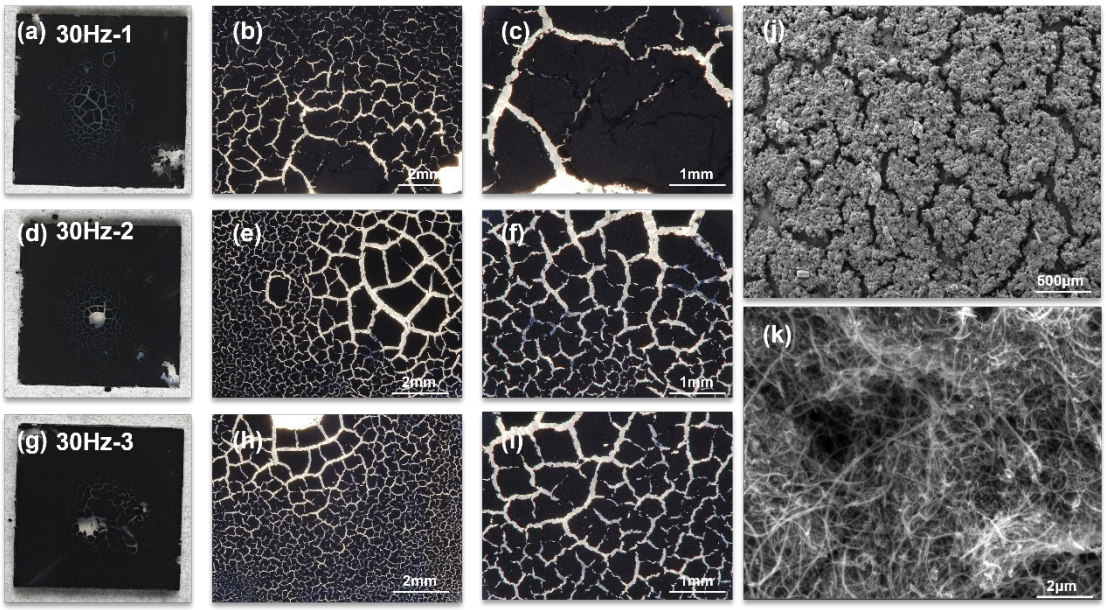

Fig. S1. Morphological images of three COOH-CNTs samples at 30 Hz vibration frequency. (a–c) Optical microscope morphology of 30 Hz-1 sample, (d–f) optical microscope morphology of 30 Hz-2 sample, (g–i) optical microscope morphology of 30 Hz-3 sample, (j–k) SEM images of COOH-CNTs sample at 30 Hz vibration frequency.

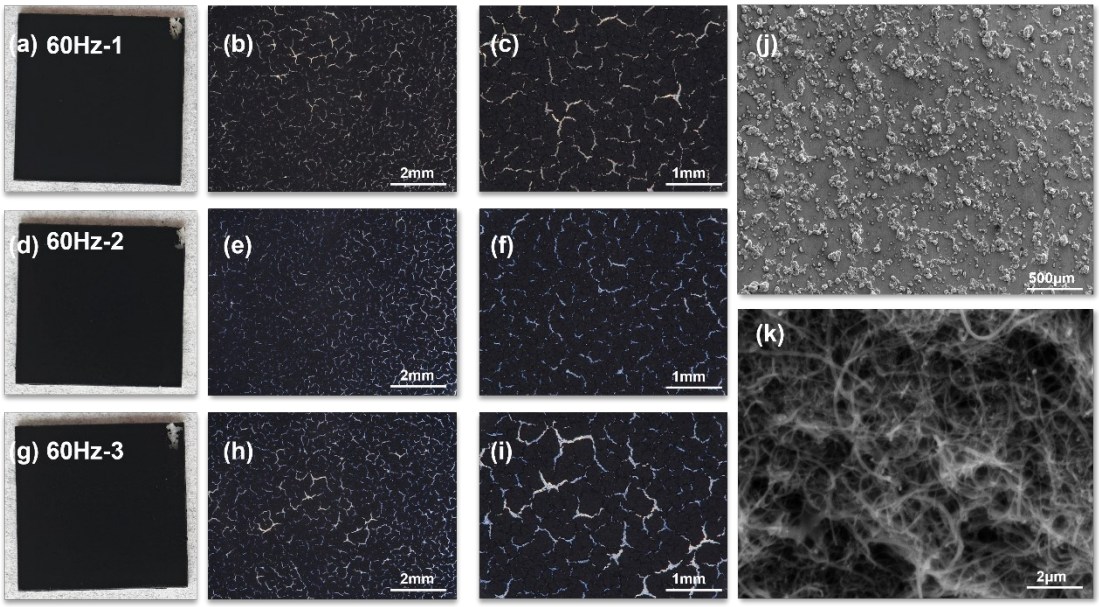

Fig. S2. Morphological images of three COOH-CNTs samples at 60 Hz vibration frequency. (a–c) Optical microscope morphology of 60 Hz-1 sample, (d–f) optical microscope morphology of 60 Hz-2 sample, (g–i) optical microscope morphology of 60 Hz-3 sample, (j–k) SEM images of COOH-CNTs sample at 60 Hz vibration frequency.

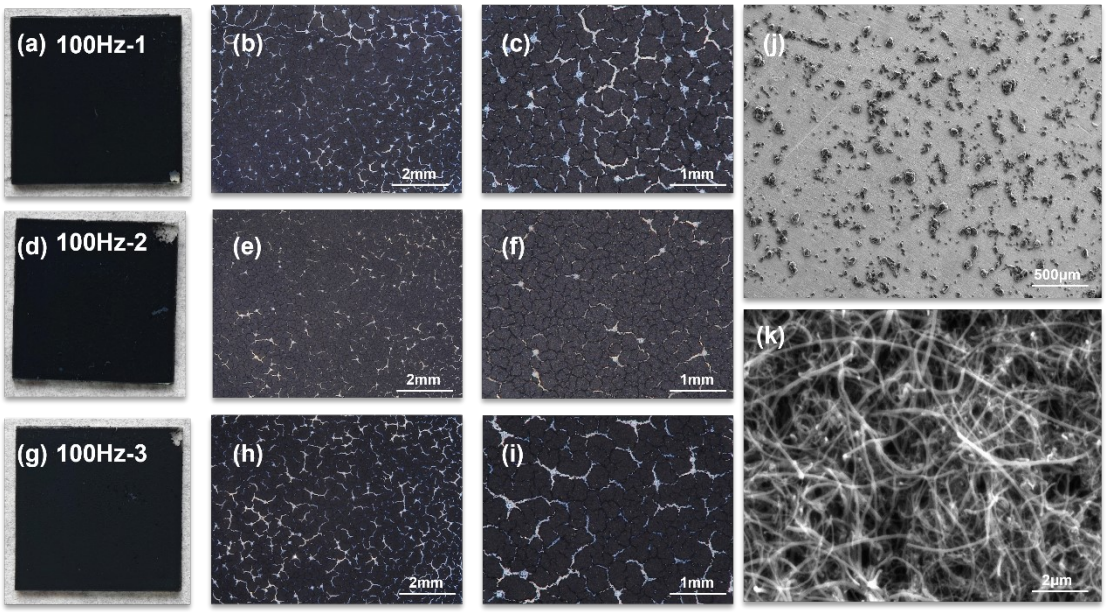

Fig. S3. Morphological images of three COOH-CNTs samples at 100 Hz vibration frequency. (a–c) Optical microscope morphology of 100 Hz-1 sample, (d–f) optical microscope morphology of 100 Hz-2 sample, (g–i) optical microscope morphology of 100 Hz-3 sample, (j–k) SEM images of COOH-CNTs sample at 100 Hz vibration frequency.

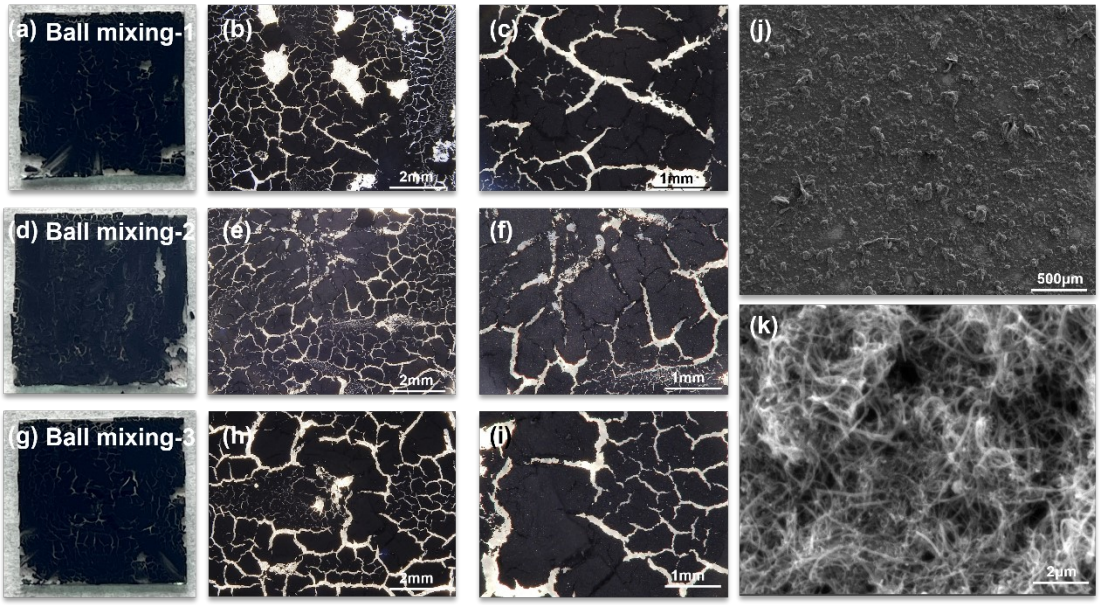

Fig. S4. Morphological images of three COOH-CNTs samples after ball mixing treatment. (a–c) Optical microscope morphology of ball mixing-1 sample, (d–f) optical microscope morphology of ball mixing-2 sample, (g–i) optical microscope morphology of ball mixing-3 sample, (j–k) SEM images of COOH-CNTs sample after ball mixing treatment.

Furthermore, to enhance the readability of SEM images while quantitatively analysing the agglomeration degree of COOH-CNTs, we employed ImageJ image analysis software to conduct particle size analysis on SEM images of samples with vibration frequencies of 30 Hz (Fig. S1(j)), 60 Hz (Fig. S2(j)), and 100 Hz (Fig. S3(j)), as well as ball milling sample (Fig. S4(j)). Fifty randomly selected CNT aggregates were counted in each SEM image to determine their particle size, yielding the respective particle size distribution diagrams. The specific results are presented in Fig. S5. It can be observed that, compared to samples treated with acoustic resonance mixing, ball mixing samples exhibit significantly larger COOH-CNTs agglomerates, with an average agglomerate diameter reaching 95.931 μm. Conversely, for samples prepared via acoustic resonance mixing, agglomerate size shows a marked decreasing trend with

increasing vibration frequency (from 65.224 μm to 21.105 μm). These data correlate with SEM image observations and simulation analyses, further demonstrating the superiority of acoustic resonance mixing technology in enhancing the dispersibility of COOH-CNTs.

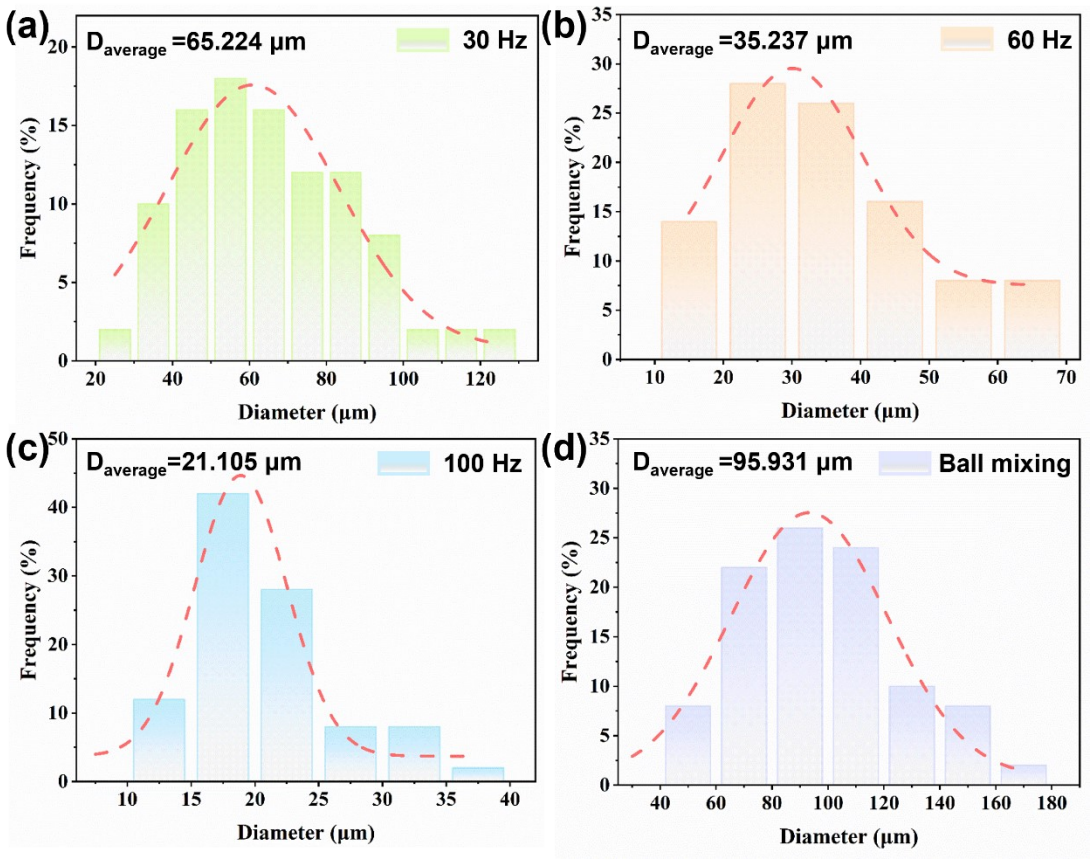

Fig. S5. Particle size distribution of COOH-CNTs following treatment with different vibration frequencies and ball milling. (a) COOH-CNTs after treatment at a vibration frequency of 30 Hz, (b) COOH-CNTs after treatment at a vibration frequency of 60 Hz, (c) COOH-CNTs after treatment at a vibration frequency of 100 Hz, (d) COOH-CNTs after ball milling.

2. Field emission testing

Fig. S6 depicts the physical composition and emission schematic of the field emission system.

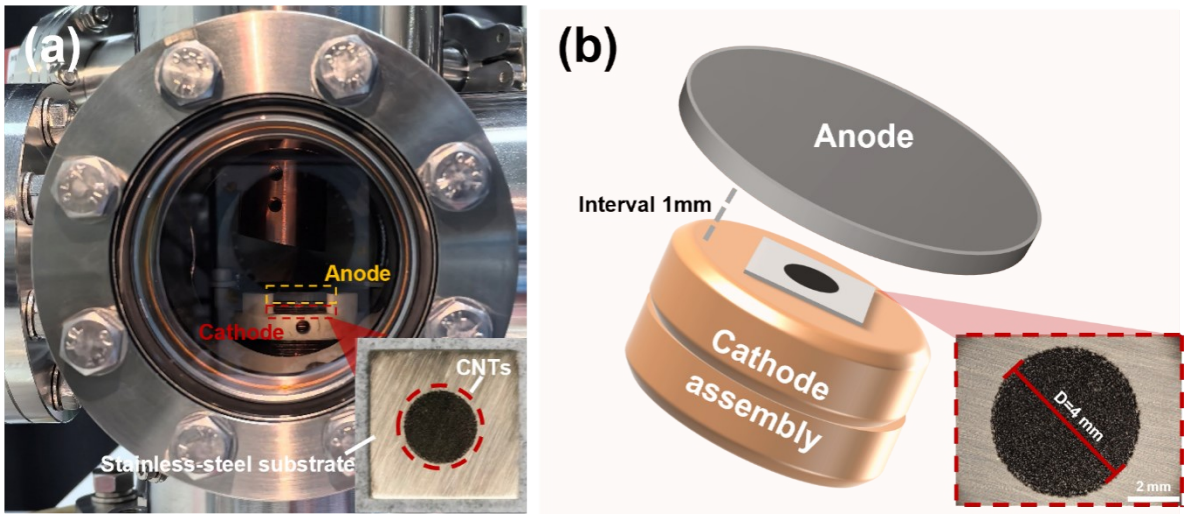

Fig. S6. (a) Field emission testing physical diagram, (b) field emission testing schematic diagram.

When analyzing the correlation between the turn-on field and β, we solved for the A_e using Eq. 3. The specific data conversion and calculations are as follows:

In this study, the E-J curve was plotted using the surface area of the sample to calculate current density(J). To analyze the correlation between the turn-on field and β, we solved for the Ae using Eq. 3. We strictly followed the formula definition (as shown in Eq. S1) to convert from E-J to E-I. The converted results are shown in Fig. S7.

$$I = J \times A_{surface} \#S1$$

Where I is the actual emission current, $A_{surface}$ is the surface area of the sample.

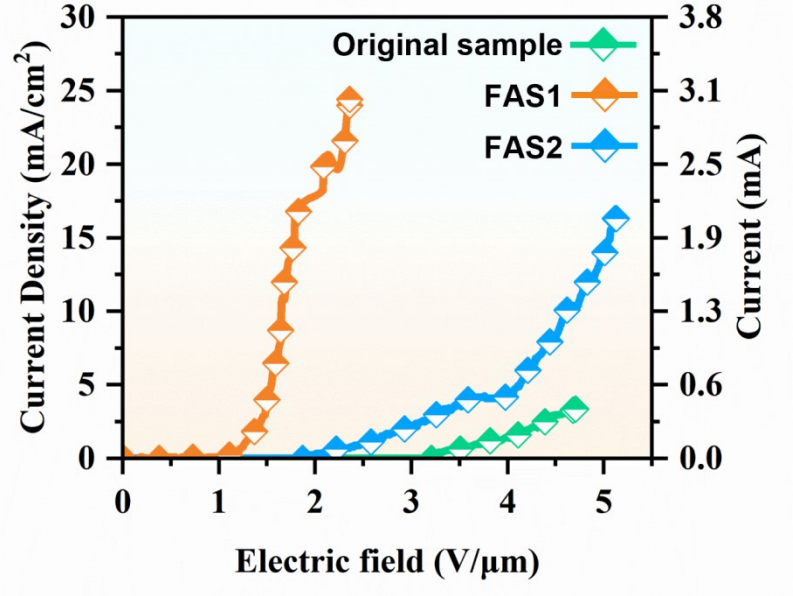

Fig. S7. (a) J-E(left) and I-E(right) curve of samples with different annealing temperatures under function-directed annealing strategy.

Based on this, we calculated the effective emission area A_e.

$$A_e = \frac{e^a \phi}{A\beta^2} \#S2$$

Where A is a constant, and a is the y-intercept of the F-N plot.

To verify the reliability of the experimental results, under the test voltage range of 0-4 kV, we conducted three independent field emission repetition experiments on the original sample, FAS1 and FAS2 respectively, in order to ensure the rigor of the research results. The experimental results are shown in Fig. S8 and Table S1.

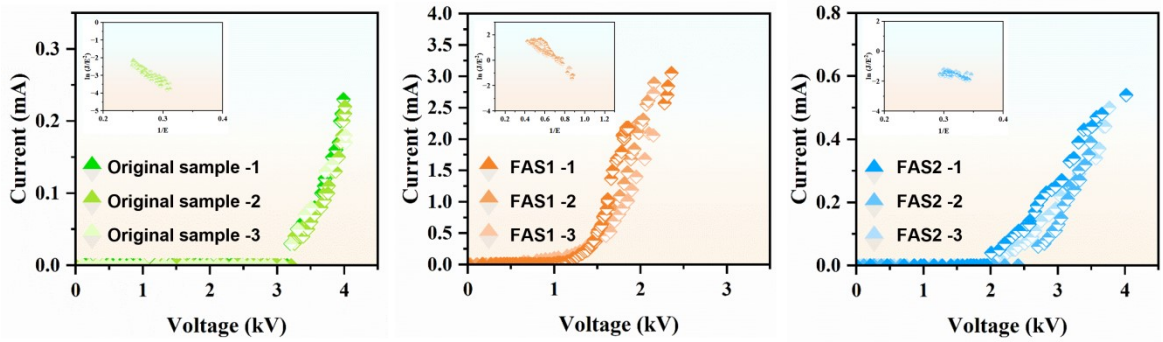

Fig. S8. The I-V curves of the original sample, FAS1 and FAS2 under the test voltage range of 0-4 kV.

Table S1

Field emission performance of original sample and samples annealed at different temperatures under the test voltage range of 0-4 kV.

Sample	E_{to} (V/μm)	E_{th}(V/μm)	I_{max} (mA)	β
Original sample -1	2	3.72	0.25	4628
Original sample -2	2.1	3.82	0.25	4489
Original sample -3	2	3.74	0.25	4613
FAS1 -1	1	1.26	3.125	9203
FAS1 -2	1.2	1.27	3.125	8923
FAS1 -3	1.1	1.26	3.125	9193
FAS2 -1	1.65	2.5	0.5	12833
FAS2 -2	1.66	2.7	0.5	12319
FAS2 -3	1.71	2.88	0.5	11732